

Neural electron backscatter diffraction

I-Tzu Huang^a, Marat I. Latypov^{a,b,*}

^aDepartment of Materials Science and Engineering, University of Arizona, Tucson, AZ 85721, USA

^bGraduate Interdisciplinary Program in Applied Mathematics, University of Arizona, Tucson, AZ 85721, USA

Abstract

In a polycrystalline microstructure, orientation and dislocation content vary smoothly within grains, and the grain boundaries between them are continuous curves. Electron backscatter diffraction (EBSD) records this continuum on a discrete grid with every subsequent analysis (from indexing to advanced pattern processing) confined to that grid. We introduce neural EBSD, which treats an EBSD scan as a continuous, differentiable four-dimensional field of Kikuchi diffraction intensity (in specimen–detector domain) and then represents it with a coordinate-based neural network. We develop and compare two formulations: a joint formulation that maps all four coordinates to intensity, and a factorized formulation that combines continuous specimen-domain coefficient fields with learned detector-domain basis patterns. Tested on recrystallized and additively manufactured Inconel 718, the factorized formulation shows better accuracy in reconstructing Kikuchi patterns that have map-averaged errors below 1% of the maximum intensity. Beyond reconstruction, it provides full-pattern super-resolution in the specimen frame, continuous querying along arbitrary off-grid paths, as well as spatially continuous boundary and heterogeneity localization from analytical spatial derivatives. Storing the network weights and learned bases in place of the raw patterns in a large dataset offers a 700-fold compression while preserving on-demand access to the full patterns for downstream analyses.

Keywords: Electron backscatter diffraction; Kikuchi patterns; Implicit neural representation; Factorized neural representation; Differentiable characterization; Polycrystalline materials

1. Introduction

In electron backscatter diffraction (EBSD), a focused electron beam scans the surface of a crystalline material and produces a Kikuchi diffraction pattern for each scan point [1]. The Kikuchi pattern contains rich information on the local structure: lattice parameters, lattice distortions (e.g., from defects), crystallographic symmetry and orientation [1, 2]. Collected over a representative surface area, the quantities derived from the patterns constitute a map of the mesoscale microstructure that enables its quantitative analysis and relation to processing or properties.

Most common EBSD analysis of single-phase materials focuses on the extraction of crystallographic orientations by indexing Kikuchi patterns

with Hough transform [3, 4, 2] or more advanced dictionary methods [5]. Resulting orientation maps allow grain segmentation (by disorientation thresholding) [6], calculation of geometrically necessary dislocation (GND) densities [7] or their proxy – kernel average misorientation (KAM) [8, 9], and grain boundary character distributions [10]. Beyond orientation, pattern-based analysis such as the image quality [8], pattern sharpness [11], or cross-correlation [12] provide additional information on local lattice (im)perfection and total dislocation content.

Recent data-driven approaches treat Kikuchi patterns in their entirety rather than reducing each pattern to a few extracted quantities. Linear methods based on multivariate statistical analysis, such as principal component analysis (PCA) or non-negative matrix factorization, express the patterns in a dataset as combinations of a finite number of principal components, which enables

*corresponding author

Email address: latmarat@arizona.edu (Marat I. Latypov)

grain segmentation without indexing [13, 14, 15, 16] or accelerated dictionary indexing [17]. Nonlinear representations have been pursued with variational autoencoders, which compress each pattern into a low-dimensional latent code that can reconstruct the original pattern with high fidelity [18, 19]. These latent-space representations support microstructure segmentation [20] and physical interpretation of individual latent dimensions [21].

Whether classical indexing of Kikuchi patterns, advanced dislocation density estimation, or latent representation by variational encoders, all EBSD analysis workflows to date share the same fundamental limitation: they are confined to discrete and often coarse grids. Yet, the underlying microstructural attributes – orientation, dislocation density, grain boundaries – are intrinsically continuous within grains and along boundary curves with discontinuities confined to grain and phase boundaries themselves. Since EBSD resolution in practice is often limited by the tradeoff with the area coverage and the acquisition time, maps obtained in existing EBSD analyses are often crude discrete approximations of continuous microstructure fields.

The following examples illustrate the limitations. First, a gentle orientation gradient probed at a significant spacing will be erroneously captured as a step change and may lead to a fictitious grain boundary identified with conventional thresholding of disorientation. Second, grain boundary identification by thresholding is only possible between grid points, which leads to highly segmented (staircase) approximations of continuous grain boundaries. Such approximation can impact the accuracy of grain boundary character distributions or chord length analysis [22]. Finally, the pain from discretization is most acute for analysis involving gradients (e.g., GND density) because their finite-difference approximation can introduce substantial numerical error and noise [7].

These limitations are not unique to EBSD and are ubiquitous for data defined on grids, including regular digital images. In the field of image processing, these limitations have been addressed with implicit neural representations (INRs). INRs parameterize a signal (e.g., grayscale or color) as a continuous function of coordinates learned by a neural network. This approach gained traction in synthesis of 3D scenes with neural radiance fields [23] and 3D shape representation with signed distance functions [24]. A key methodological advance was the introduction of sinusoidal representation networks

(SIRENs) [25], whose periodic activation functions enable accurate representation of signals *and* their spatial derivatives. Unlike earlier ReLU networks, SIRENs accurately represent high-frequency signals as have been shown by successful representation of images, video, and wavefields [25, 26, 27, 28]. Compared to grid-based representations, INRs are [29, 25, 30]

1. **continuous** and resolution-agnostic, which allows querying the signal at arbitrary specimen positions;
2. **differentiable**, which provides access to analytic gradients of the signal without finite-difference approximation;
3. **significantly more** memory- and disk-efficient than raw data arrays.

These properties are especially useful for scientific applications and have already found adoption in biomedical imaging [30, 31, 32, 33]. In materials microscopy, the only published application is INR-TEM [34], in which a coordinate-based detection head identifies cavities in bright-field transmission electron microscopy images at arbitrary resolution. Developing INR for EBSD is not trivial as each grid point contains an image rather than a scalar intensity.

In this paper, we present the first demonstration of an implicit neural representation of EBSD. To address the challenge of the hierarchical nature of the data (images at grid points), we treat an EBSD map as a continuous 4D diffraction field (Figure 1) as a function of specimen coordinates (x, y) and detector coordinates (u, v) . Such view preserves spatial relationships of Kikuchi patterns and allows fitting the field with a coordinate-based neural network.

A direct realization is to learn this field with a single monolithic INR over the joint coordinate space (x, y, u, v) . However, recent studies (e.g., TensorRF [35]) have shown that high-dimensional neural fields can be represented more efficiently by factorizing the field into compact low-rank components instead of a dense or fully implicit representation. In EBSD, this tensorial perspective is especially natural because a polycrystalline pattern field can be viewed as spatially varying combinations of characteristic diffraction patterns. In this context, we explore two formulations of neural EBSD: (i) a joint formulation (4D-INR), in which a single SIREN-type network learns the diffraction in-

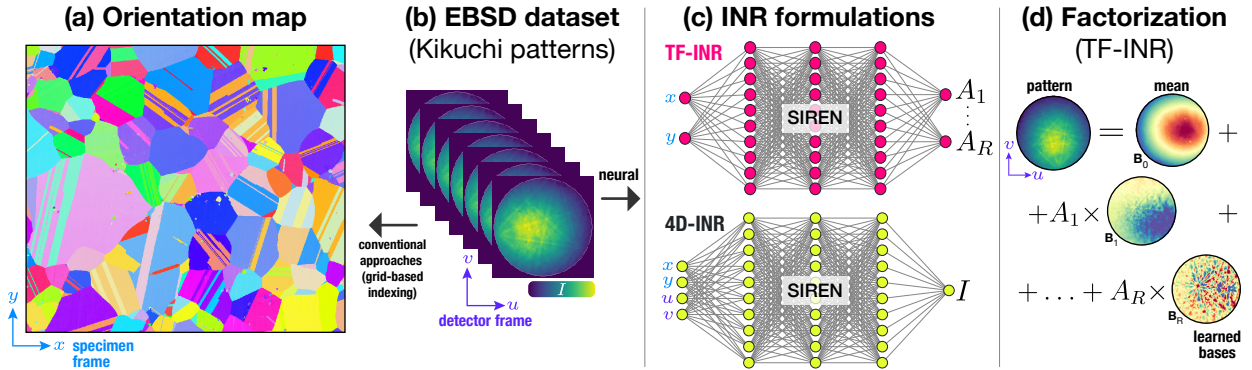


Figure 1: Overview of the present study.

tensity as a continuous function of all four coordinates (x, y, u, v) ; and (ii) a factorized formulation (TF-INR), in which a SIREN-type network learns continuous coefficient fields in the specimen domain that linearly combine a set of learnable basis patterns in the detector domain (Figure 1c).

With a case study on Ni-base superalloys, we find that the factorized formulation achieves substantially higher reconstruction accuracy than the joint formulation. We further show that neural EBSD provides a unified continuous description of EBSD that turns reconstruction, compression, and derivative-based microstructure analysis into natural consequences of the representation. Two of these capabilities are especially difficult to achieve with conventional grid-bound EBSD analysis. First, the continuity of the learned field enables sub-grid reconstruction of full Kikuchi patterns allowing full-pattern super-resolution and the tracking of diffraction evolution along arbitrary paths in the specimen frame. Second, the differentiability of the learned coefficient fields provides a practical route to boundary localization with sub-pixel spatial continuity, free of the staircase artifacts inherent to grid-based segmentation and without requiring pattern indexing.

2. Neural EBSD

2.1. EBSD as a continuous field

A key idea of this work is to treat the EBSD signal as a discrete sampling of a continuous 4D field of the Kikuchi diffraction intensity, I :

$$I = I(x, y, u, v), \quad (1)$$

where (x, y) are coordinates in the specimen frame and (u, v) are the coordinates in the detector frame. Our objective is to recover this field as a continuous, differentiable function of the specimen coordinates (x, y) so that the diffraction signal can be queried, differentiated, and analyzed at arbitrary locations. We address the spatial continuity with SIREN [25], whose differentiability can be exploited for microstructure analysis Section 3.3. In contrast, the detector domain can be approached with different strategies, which motivates the two formulations presented below and in Figure 1c.

2.2. Two formulations of neural EBSD

Our first approach to the detector domain is to consider the detector coordinates continuous, which leads to neural approximation of the intensity field, $I(x, y, u, v)$, with a single SIREN-type network, F_θ , parametrized by weights θ :

$$F_\theta : (x, y, u, v) \mapsto I. \quad (2)$$

This is the most direct realization of Equation (1) and serves as a natural baseline, which we refer to as the *joint formulation*. Although direct, this approach is non-trivial in two respects. First, four-dimensional (4D) inputs are uncommon in INR practice, where most applications operate on 2D or 3D domains [36, 37, 24, 38]. Second, with a single set of shared weights, the network must simultaneously capture the high-frequency band structure in the detector domain and a very different frequency content in the specimen domain: smooth diffraction intragranular variation with sharp transitions at grain (or phase) boundaries.

The frequency mismatch between the specimen and detector domains makes INR of EBSD maps

especially challenging so that a single network is not guaranteed to succeed even with the SIREN architecture. Two characteristics of EBSD motivate an alternative approach maintaining the detector domain discrete. First, a map of a polycrystal consists of a finite number of nearly uniform orientation patches (grains), each with a characteristic Kikuchi pattern. Second, the success of multivariate approaches, such as PCA [13] and non-negative matrix factorizations [15], as well as dictionary indexing [5, 17] shows that the diffraction signal across an entire map can be efficiently represented as a combination of relatively few characteristic patterns. These characteristics motivate the *factorized formulation* that decomposes the diffraction signal as follows:

$$I(x, y, u, v) = \sum_{r=1}^R A_r(x, y) B_r(u, v), \quad (3)$$

where $A_r(x, y)$ is the r^{th} coefficient field in the specimen domain, $B_r(u, v)$ is the r^{th} basis pattern in the detector domain, and R is the rank of the decomposition. The bases carry the characteristic diffraction patterns whose weighted combination represents the diffraction signal across the map. The coefficients $A_r(x, y)$ serve as the weights of the corresponding bases at every scan position (see Figure 1d).

With the specimen–detector decomposition, the neural representation can be pursued with a neural network that predicts coefficient fields, \mathbf{A} :

$$f_\theta : (x, y) \mapsto (A_1, A_2, \dots, A_R), \quad (4)$$

optimized jointly with the corresponding basis patterns, \mathbf{B} . The basis patterns are parameterized as R learnable weight arrays of size $H_p \times W_p$ matching the resolution of the EBSD detector screen. The detector domain is therefore represented at its native acquisition resolution, while the specimen domain is represented continuously through the learned coefficient fields $\mathbf{A}(x, y)$.

This hybrid continuous–discrete design builds on the success of similar architectures for natural-image and 3D-scene applications, where coordinate-based networks are combined with explicit grid-stored features for efficiency [35, 39]. For EBSD, this decomposition introduces the continuity in the specimen domain, where it is most useful, yet captures the finite number of characteristic patterns expected in a polycrystalline microstructure through

learnable weight arrays. PCA of Kikuchi patterns before training can guide the selection of the optimal rank, R , by identifying the number of characteristic patterns that captures a target fraction of variance (e.g., 95%) in a given EBSD dataset.

Both formulations satisfy our objective of spatial continuity in the specimen domain. Practical architectural choices with the dataset-specific implementation details are given in Section 6.

2.3. Training strategy

Both formulations are trained by minimizing a reconstruction loss over sampled specimen–detector coordinates with a few additional considerations specific to EBSD. First, since an EBSD dataset can contain hundreds of millions of intensity values across the combined 4D domain, we sample intensities from a subset of 4D coordinates, Ω , at each training iteration. Second, Kikuchi patterns contain high-frequency, narrow band edges with a slowly varying background. As band edges carry the most important information, the corresponding pixels should be emphasized during learning so that the network does not focus on easier to predict yet less informative background regions of the Kikuchi diffraction. For these reasons, we identify band regions as part of pattern pre-processing (see Section 6) and then, during training: (i) introduce weights, $w(u, v) \geq 0$, that emphasize the intensity at band-region pixels and (ii) bias the sampling to include more band-region pixels in the Ω subsets. These two measures are complementary as the sampling bias focuses training to informative regions, while pixel weighting ensures that the gradient signal from band pixels is not diluted by background pixels within a given iteration.

With these considerations, the reconstruction loss is defined as

$$\mathcal{L}_{\text{pixel}} = \frac{1}{|\Omega|} \sum_{(x, y, u, v) \in \Omega} w(u, v) \times \left(\hat{I}(x, y, u, v) - I(x, y, u, v) \right)^2, \quad (5)$$

where the predicted intensity, \hat{I} , depends on the formulation:

$$\hat{I} = \begin{cases} F_\theta(x, y, u, v) & \text{(joint),} \\ \sum_{r=1}^R [f_\theta(x, y)]_r B_r(u, v) & \text{(factorized).} \end{cases} \quad (6)$$

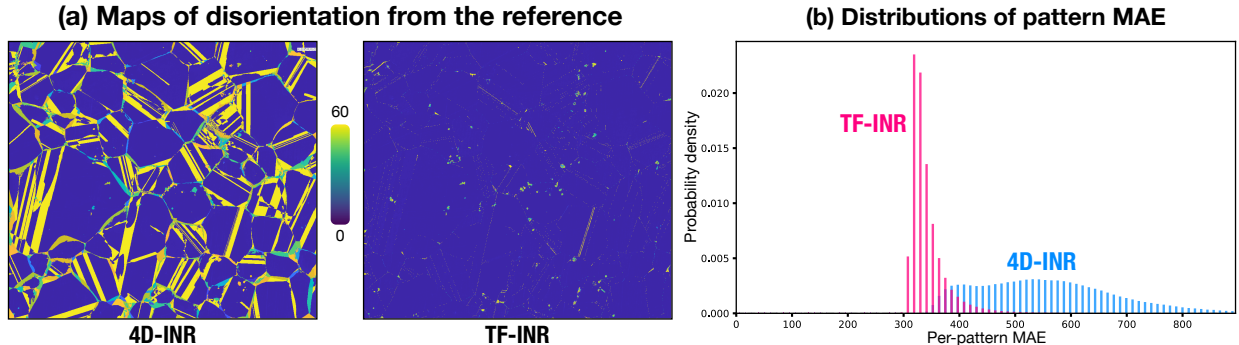


Figure 2: Reconstructions of the RX718 map with 4D-INR and TF-INR compared in terms of (a) orientation deviation maps and (b) distributions of pattern-level MAE values.

The joint formulation minimizes the reconstruction loss as the total training objective: $\mathcal{L}_{\text{total}} = \mathcal{L}_{\text{pixel}}$.

For the factorized formulation, we introduce an additional term, $\|\mathbf{B}\|_F^2$, that regularizes the basis patterns to prevent the ambiguity between (A_r, B_r) and $(cA_r, B_r/c)$ for any $c \neq 0$ in Equation (3):

$$\mathcal{L}_{\text{total}} = \mathcal{L}_{\text{pixel}} + \lambda_B \|\mathbf{B}\|_F^2, \quad (7)$$

The term $\lambda_B \|\mathbf{B}\|_F^2$ penalizes large basis-pattern magnitudes and thus prevents the optimizer from inflating B_r while shrinking A_r during training ($\|\cdot\|_F$ is the Frobenius norm).

Training is performed for each individual EBSD dataset by adjusting: (i) SIREN weights θ in the joint formulation; (ii) both SIREN weights θ and basis-pattern weights \mathbf{B} in the factorized formulation.

3. Results: Neural EBSD of superalloys

We demonstrate the framework on EBSD datasets for polycrystalline Ni-base superalloys obtained and published by Calvat et al. [21]. Specifically, Inconel 718 alloys in two distinct microstructure states were considered here (RX and AM) to sample microstructural diversity that should be handled by the neural EBSD framework. RX718 is a recrystallized wrought IN718 alloy with well-defined grains and sharp boundaries; AM718 is an additively manufactured IN718 alloy (direct energy deposition) in as-built condition with less distinct boundaries, intragranular heterogeneity, and the elevated defect content. Each map covers 0.9 mm^2 surface area at a $1 \mu\text{m}$ step (9×10^5 patterns), which

tests the scalability of the neural representation beyond sizes of typical EBSD maps. We train on the 120×120 patterns as 16-bit images provided with the dataset, which preserve the characteristic diffraction features of original 480×480 images at reduced computational cost. The acquisition details are given in Section 6 as well as in Calvat et al. [21, 18]. Both formulations were trained per map and showed stable convergence. For TF-INR, we used the rank $R = 512$ for both maps guided by PCA of the measured patterns (Figure 8a) and the trade-off between the reconstruction accuracy and computational cost.

Two-level evaluation. We assess the fidelity of trained neural representations against the original measurements at two levels. At the pattern level, we use the mean absolute error (MAE): the absolute difference between the reconstructed and measured Kikuchi patterns averaged over the detector pixels within the aperture mask (Equation (9), Figure 8b). The map-averaged MAE is the mean of pattern MAE over all scan positions (Equation (10)). MAE is reported in 16-bit intensity counts; dividing by the dataset-wide maximum intensity (61 183 for RX718, 58 727 for AM718) gives the error as a percentage of full scale.

At the orientation level, we index both the reconstructed and measured patterns with conventional Hough-transform algorithms (implemented in *kikuchipy* [40, 41]) and compute the symmetry-reduced disorientation angle between the two orientations (using MTEX [42, 43]). We refer to this angle as the orientation deviation (Equation (11)). It quantifies the impact of reconstruction errors on the indexed orientation as the most common output of EBSD analysis. The orientation deviation

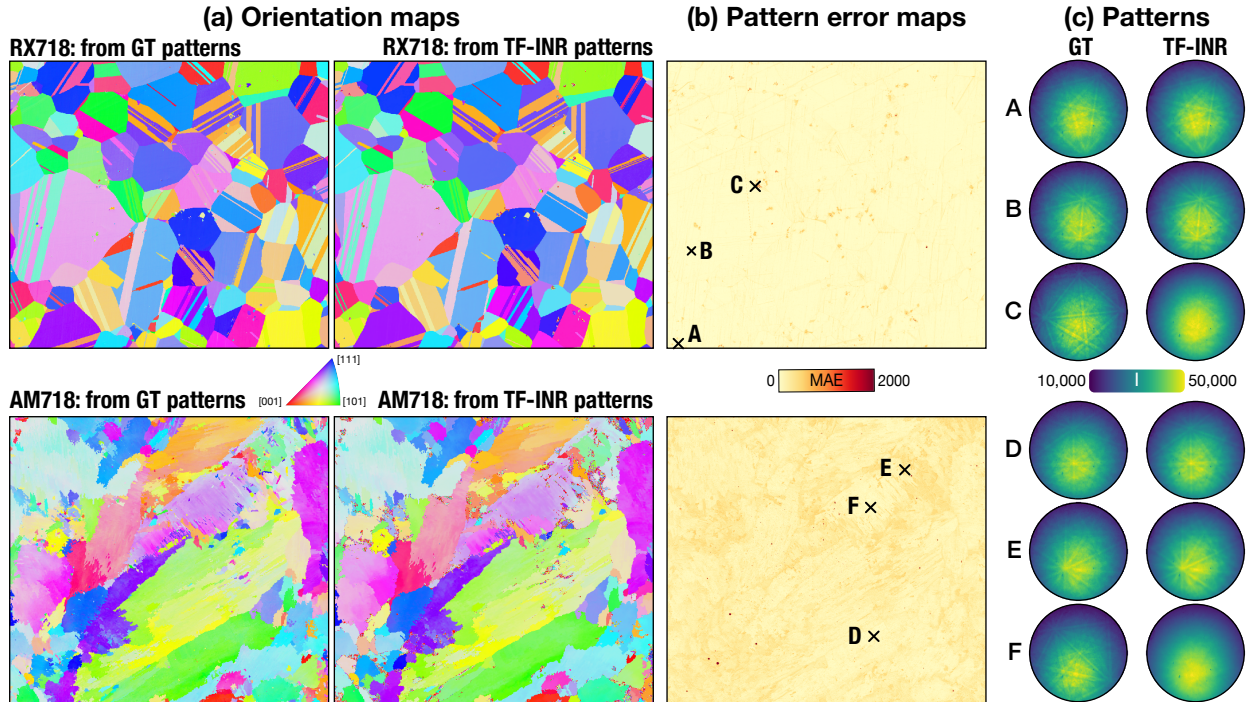


Figure 3: Reconstruction of EBSD data evaluated in terms of (a) orientation maps obtained with Hough indexing of measured (GT) Kikuchi patterns and those reconstructed from TF-INR and (b) error maps showing pattern-level MAE (Equation (9)). Visual comparison of (c) measured and reconstructed patterns for selected grid points are also shown corresponding to locations with both low and high pattern-level MAEs.

isolates errors of crystallographic significance from those affecting only absolute detector-pixel intensities.

As both error metrics are computed for each grid point, (x, y) , the reconstruction accuracy for an EBSD dataset is reported through statistical summaries, distributions, and maps. Statistical summaries include map-averaged values and fractions of the grid points with an error metric below (or above) a threshold: e.g., fraction of grid points with the orientation deviation below 4° based on the definition of "small" disorientation introduced elsewhere [44].

3.1. Reconstruction

4D-INR vs TF-INR. We first benchmark the joint and factorized formulations on the RX718 map, where the well-defined recrystallized grain structure provides a clean test of reconstruction fidelity. The two formulations produce significantly different reconstructions (Figure 2). The 4D-INR baseline yields a broad MAE distribution shifted toward higher reconstruction errors (Figure 2b), and its

orientation deviation map shows angular errors extending across grain interiors. A large fraction of grid points, 19.1%, exceeds the 4° threshold. TF-INR, in contrast, produces a narrow MAE distribution in a lower-value range and a uniform orientation deviation map with errors concentrated at grain boundaries. The fraction of grid points with orientation deviation $\geq 4^\circ$ is only 1.2% (of 9×10^5 orientations). Since TF-INR offers a much more faithful reconstruction, we focus on this formulation for the rest of this study.

The reconstruction fidelity of TF-INR is next examined for both microstructures, RX718 and AM718, in terms of indexed orientation maps, MAE maps, and visual inspection of selected individual patterns (Figure 3). The orientation maps (from reconstructed patterns) closely match the reference orientation maps (from measured patterns) for both microstructures. The map-averaged MAE values are 344 and 483 intensity counts for RX718 and AM718, which correspond to normalized MAE of 0.6% and 0.8% relative to the dataset-wide maxima. The spatial distribution of the residuals mirrors the microstructural complexity of each sam-

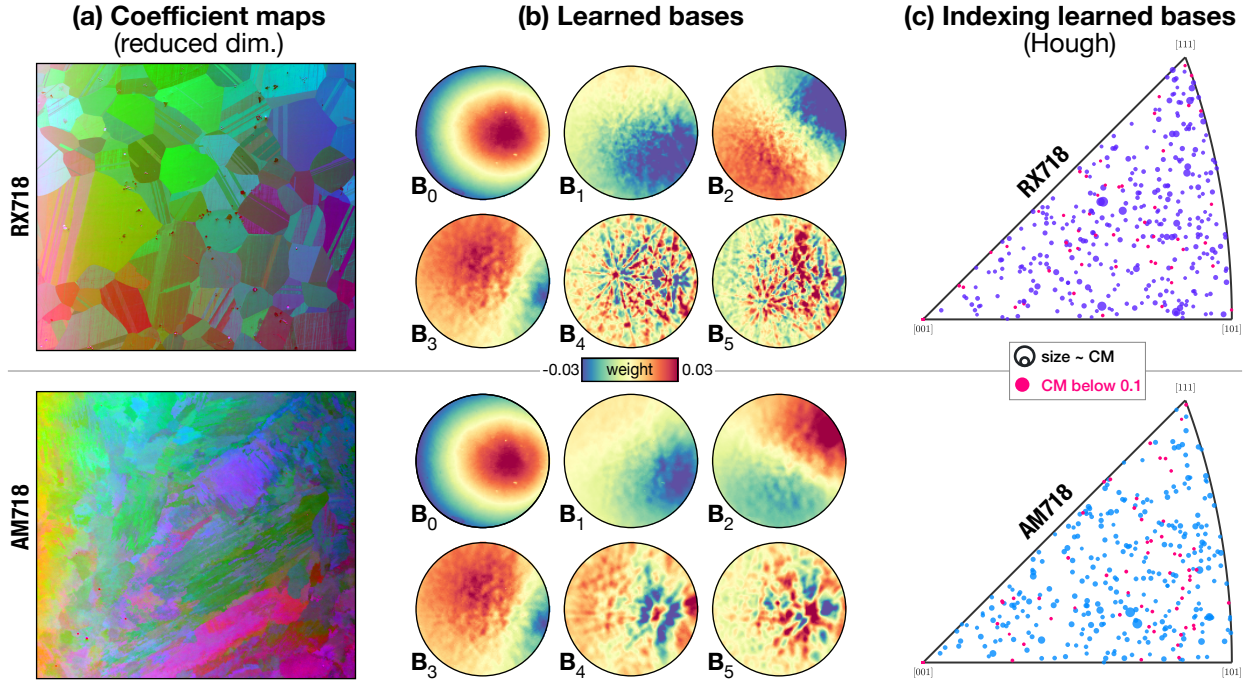


Figure 4: Learned TF-INR representation: (a) coefficient field $\mathbf{A}(x, y)$ projected from $R = 512$ to three dimensions with PCA shown with RGB; (b) examples of learned bases, \mathbf{B}_r ; (c) 512 crystallographic orientations obtained by Hough indexing of the learned bases (circle size is proportional to indexing confidence metric, orientations obtained with confidence metric below 0.1 are shown in red).

ple. In RX718, the larger errors in both intensity and indexed orientation are confined to small grains/particles and grain boundaries. In AM718, the residuals are more uniformly distributed and reach into the grain interiors, consistent with its stronger intragranular heterogeneity. The representative patterns in Figure 3c show examples of grid points with low and high MAE. The low-MAE patterns (A, B, D, E) display excellent agreement in both the Kikuchi-band configuration and intensity. At the high-MAE points (C, F), the TF-INR model predicts mostly background intensity with weak bands, whereas the measured patterns have clear bands.

Given strong reconstruction performance of TF-INR on both maps, we inspect the learned representation by visualizing the coefficient fields and selected basis patterns (Figure 4). The coefficient field $\mathbf{A}(x, y)$ contains a 512-dimensional vector at every grid point. To visualize the field, we project the coefficients to three dimensions by PCA and map the result to RGB (Figure 4a). The projection shows spatially coherent regions corresponding to the grain structure in both alloys (compare

with Figure 3a). It means the continuous spatial field has captured the piecewise-smooth organization of the polycrystalline microstructure without being explicitly given any orientation or boundary information. Many of the learned bases \mathbf{B}_r resemble Kikuchi patterns instead of being abstract (Figure 4b). The leading basis (\mathbf{B}_0) is smooth (and similar to background intensity distribution) because it is initialized from the mean pattern over the dataset (its coefficient, A_0 , is fixed to unity). Other bases include finer band structures that appear as realistic diffraction patterns bearing crystallographic orientations. Indeed, Hough-indexing of the bases (like regular Kikuchi patterns) results in valid orientations with confidence metric (see Section 6) above 0.1 for many of the 512 bases (Figure 4c).

3.2. Continuous query of the diffraction field

A unique advantage of the neural representation is that Kikuchi patterns can be reconstructed at arbitrary specimen coordinates not restricted to the original measurement grid. Here, we provide two demonstrations of this property: (i) coarse-grid super-resolution: reconstruction of Kikuchi pat-

terns on a fine grid from sparse sampling, and (ii) sub-grid path sampling: pattern evolution along arbitrary paths with sub-grid resolution.

Coarse-grid super-resolution. We first test the capability of the TF-INR model to upscale coarse-grid measurement to a high-resolution grid. To this end, we re-trained the TF-INR model using only every other scan position in both horizontal and vertical directions of each map. For 900×1000 maps, using only a quarter of points reduces the number of scan positions available for training to 225 000. The remaining 675 000 positions were unseen by the model and used only for evaluation. After training on this sparse grid, TF-INR was queried at the withheld positions to reconstruct the missing patterns and evaluated in terms of orientation deviation with the same procedure as for the full-grid reconstruction (Section 3).

Despite being trained on only 25% of the original scan positions, TF-INR successfully recovers the withheld patterns with high accuracy in terms of indexed orientation. For RX718, 97% of the held-out points were reconstructed within 4° of the reference orientation, with a mean orientation deviation of 0.9° . For AM718, the corresponding fraction was 89%, with a mean orientation deviation of 4.7° . The lower accuracy in AM718 is consistent with its more heterogeneous microstructure, stronger intragranular orientation variation, and larger population of mixed patterns associated with boundaries or defect substructure. Nevertheless, the result shows the potential of TF-INR to upscale EBSD maps at Kikuchi pattern level from coarse measurements with only 3% of fine-grid points having non-small deviations in terms of the crystallographic orientation (as demonstrated by the RX718 case).

Sub-grid path sampling. To probe TF-INR at resolutions finer than the original measurement step, we queried the learned field at four equally spaced positions between adjacent grid points. This sub-grid sampling corresponds to five-fold refinement in spatial resolution along a chosen path. Each pair was selected to span two grains to analyze how the model handles sharp orientation changes at sub-grid scale. This is the regime most relevant to grain boundary characterization, where conventional grid-based analysis is intrinsically limited by the measurement resolution. Two path orientations were considered for each microstructure: horizontal (aligned with one of the scan axes) and diagonal (not aligned with the scan axes).

Along each path, the reconstructed patterns

transition smoothly from one endpoint to the other (Figure 6a,b). Diffraction features associated with the first grain progressively weaken while features of the second grain emerge. This behavior is consistent with physical diffraction across a grain boundary [45, 46]. The transition is non-uniform along the path, which is seen from visual inspection of the patterns and with the indexing confidence metric (Figure 6c). The confidence metric is low when the Hough peak structure is ambiguous, including the overlap of patterns due to contributions of two (or more) grains at a grain boundary [46, 47]. Tracked for the queried patterns, the confidence metric exhibits a dip along three of the four paths. In each case, the dip is off the path midpoint. Since confidence drops where patterns mix contributions from neighboring grains, the minimum in the curve likely marks a boundary at sub-grid resolution. The diagonal path in the RX718 case (B-B in Figure 6a,c) shows that the low-confidence region is not necessarily confined to a single sub-grid point. These results suggest the potential of localizing grain boundaries in a continuous fashion in the specimen frame (pursued in the next section).

The remaining path in AM718 (C-C in Figure 6b,c) exhibits a different behavior. The TF-INR reconstruction at one endpoint of this path has a relatively high error (MAE = 432) compared to the rest of the map and produces a low-confidence pattern despite high confidence in indexing the measured pattern at the same position (see light stand-alone circle in Figure 6c). Along the path, the model recovers patterns of progressively higher confidence towards the other endpoint (Figure 6b). This result demonstrates smooth behavior of the continuous representation even in a scenario of locally imperfect reconstruction.

Based on these results, TF-INR, as a continuous representation of the diffraction field, allows pattern-level upscaling from coarse measurement grids and tracking pattern evolution across grain boundaries at scales much finer than the original step size.

3.3. Continuous and indexing-free grain boundary localization

The differentiability of the neural EBSD representation enables a new approach to grain boundary localization and visualization. Instead of pixel-wise thresholding of disorientations on a discrete grid, boundaries can be localized directly from analytical spatial derivatives in the specimen domain.

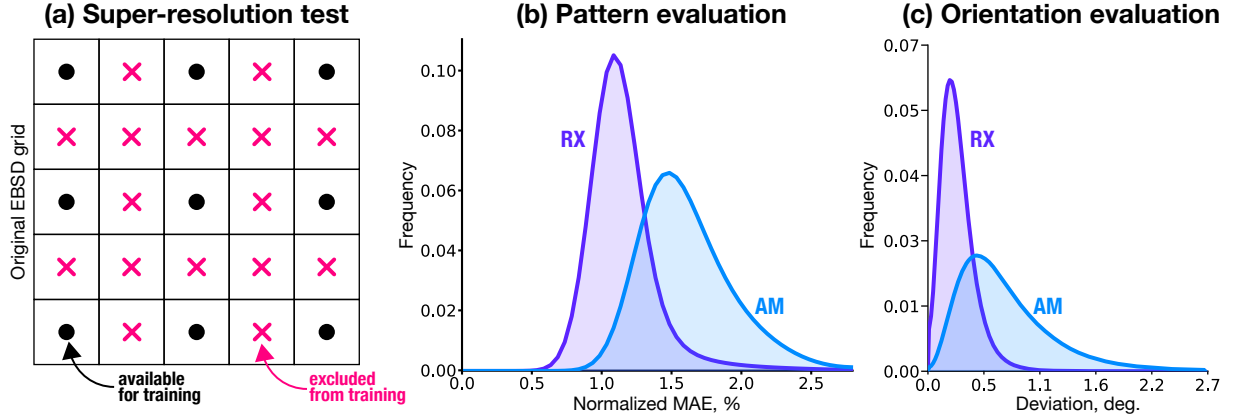


Figure 5: Demonstration of super-resolution: (a) hold-out of every other pixel (red cross) during training to emulate coarse-grid experimental measurement (black circles); (b) distributions of normalized MAE values for 6.75×10^5 held-out grid points; (c) distributions of orientation deviations from reference orientations at held-out grid points.

For TF-INR specifically, we introduce the diffraction gradient field expressed as

$$S(x, y) = \sqrt{\sum_{r=1}^R \left[\left(\frac{\partial A_r}{\partial x} \right)^2 + \left(\frac{\partial A_r}{\partial y} \right)^2 \right]} = \|\nabla_{x,y} \mathbf{A}\|_F, \quad (8)$$

which quantifies the magnitude of spatial variation of the coefficient field, $\mathbf{A}(x, y)$. Since $\mathbf{A}(x, y)$ are represented by a SIREN, the gradients $\nabla_{x,y} \mathbf{A}$ are accessible analytically by automatic differentiation without the need for finite-difference approximation, which is susceptible to noise that plagues gradient-based analyses on conventional EBSD grids.

From Equation (8), the magnitude of the gradient is high when there is a significant change in the coefficients \mathbf{A} , which reflects sharp discontinuity of the diffraction field in the specimen domain. Such discontinuities are expected at grain (or other) boundaries and locations with changes in the lattice defect content. The field, $S(x, y)$, thus offers a new route for indexing-free localization of grain boundaries and other defects that can be visualized with any resolution.

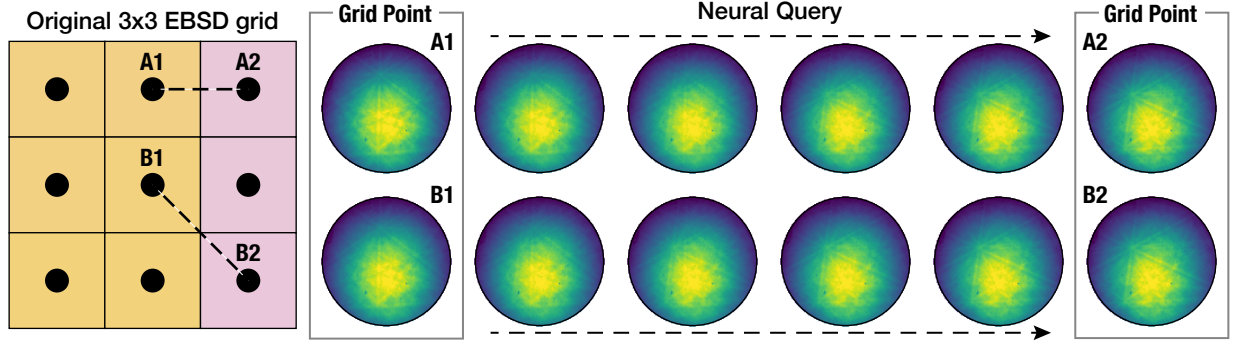
Visualized for RX718 and AM718 microstructures, the diffraction gradient maps exhibit boundary networks largely consistent with the grain boundaries obtained based on disorientations [6]. While most conventional workflows for grain segmentation and boundary visualization rely on discrete thresholds (e.g., 2° , 10° as shown in Figure 7a), the diffraction gradient is intrinsically con-

tinuous and does not require selection of a threshold.

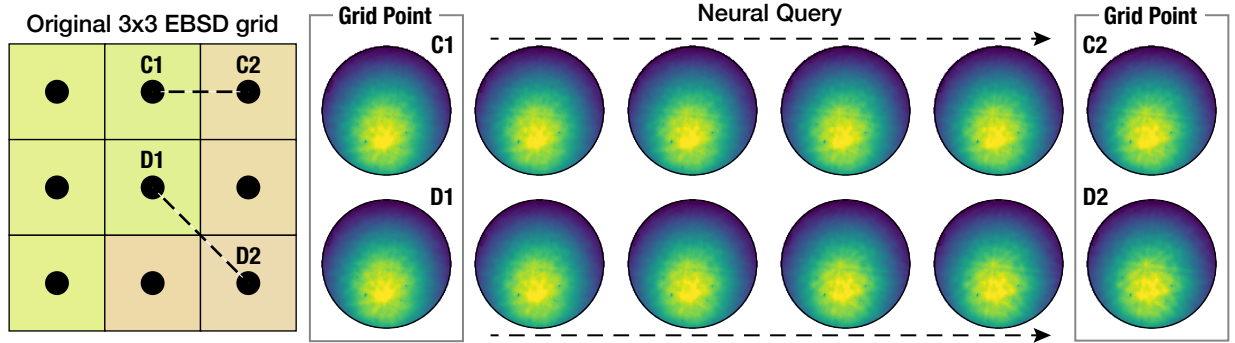
The continuous diffraction gradient reveals that the discontinuity magnitude is non-uniform even along a single grain boundary with variations along its trace (Figure 7). Most segmentation workflows used in practice only detect the presence of a boundary for a chosen threshold and discard this variation, even though the underlying disorientation is continuous [48]. The diffraction gradient map reveals these variations explicitly with a single scalar without the need for advanced coloring schemes. Since S captures the full change in the diffraction patterns not limited to the orientation (e.g., sharpness), the variation along the boundary may reflect subtle changes in the grain boundary character (e.g., inclination) or its defect content. The diffraction gradient also localizes boundaries of particles, some with clean interiors, some filled with high S (Figure 7b, gray arrows). The high- S regions could correspond to particles with rough surfaces and deteriorated or significantly varying patterns within their areas.

The continuously varying magnitude also reveals intragranular heterogeneities. In the RX718 case, the diffraction gradient field exhibits cross-hatched patterns of slightly elevated magnitude. Based on the corresponding image quality maps, these features are associated with lattice defects introduced with remnant polishing scratches. In contrast, polishing scratches (some of which are conventionally segmented as low-angle grain boundaries, see arrow in the AM718 map in Figure 7) do not appear in the diffraction gradient maps for AM718. The

(a) Sub-grid query in RX718



(b) Sub-grid query in AM718



(c) Indexing confidence and diffraction gradient along the paths

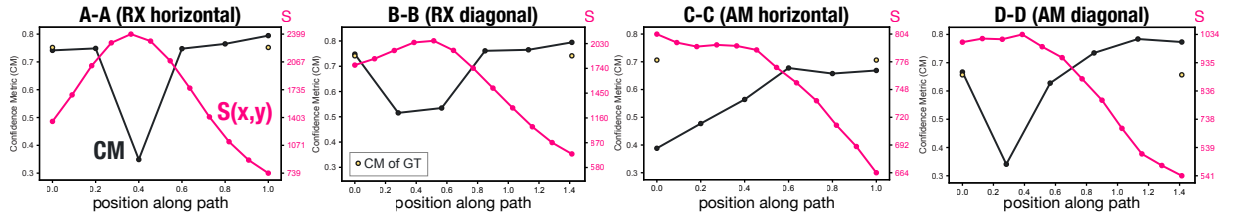


Figure 6: Demonstration of sub-grid path sampling: (a-b) sub-grid query between EBSD pixels in two directions in RX718 and AM718 microstructures; (c) indexing confidence and diffraction gradient (Section 3.3) along the paths. See Figure 8c for the locations of the 3×3 grids shown here.

exposure of intragranular heterogeneity is most evident in AM718. For this microstructure, the diffraction gradient map reveals high-angle grain boundaries, consistent with the conventional thresholding, a network of low-angle grain boundaries, as well as elevated gradient magnitudes throughout the grain (and subgrain) interiors. The elevated magnitudes most likely originate from dislocation cells reported for this alloy in the as-built condition [18].

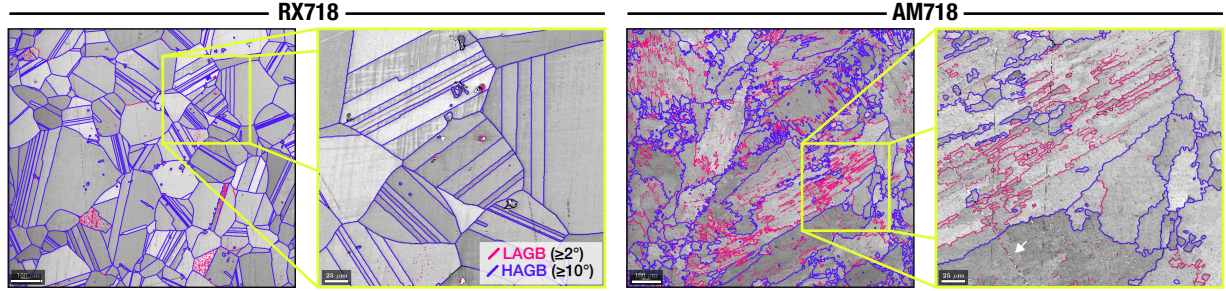
The gradient field is also continuous in the specimen domain and can be sampled with automatic differentiation on grids of any resolution. As alluded in the previous section, this property allows localizing grain boundaries in a spatially continuous fashion beyond grid midpoint positions or staircase-

like approximations characteristic of grid-based segmentation. The boundary continuity is illustrated in the diffraction gradient profiles for the same paths analyzed in Figure 6. These profiles shows peaks in the same off-midpoint positions as dips in the confidence metric (Figure 6c).

4. Discussion

Neural EBSD changes the object of analysis: instead of a discrete set of independent patterns, an EBSD measurement becomes a continuous diffraction field that can be queried and differentiated anywhere in the spatial domain. This representation

(a) Grain boundaries from disorientation-based segmentation



(b) Diffraction gradient field

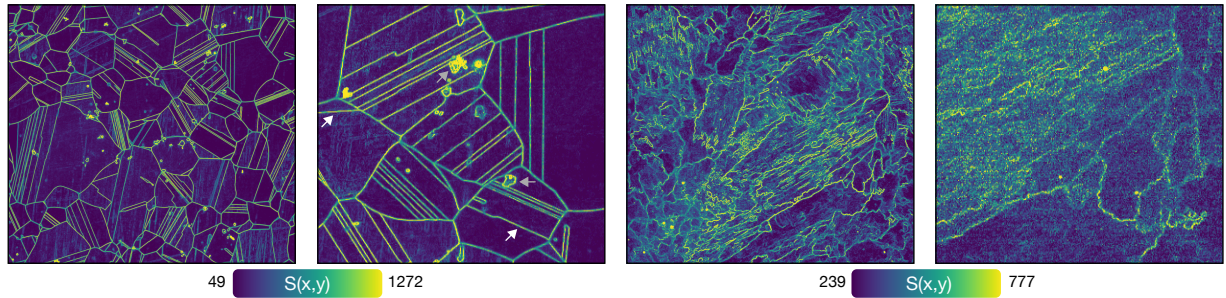


Figure 7: Grain boundary analysis for RX718 and AM718 microstructures: (a) conventional disorientation-based segmentation and (b) diffraction gradient field from differentiation of the coefficient field (Equation (8)). Grain boundaries in (a) are shown for two thresholds: 2° (low angle, LAGB) and 10° (high angle, HAGB) overlaid with the image quality map from experimental EBSD measurement. Arrows indicate interesting features, including (i) white arrows in (b): examples of diffraction gradient varying along a single boundary; (ii) gray arrows in (b): small areas enclosed by high diffraction gradient possibly related to particles; (iii) white arrow in (a): polishing artifact detected as a LAGB with disorientation thresholding that is absent in the diffraction gradient field in (b).

offers new capabilities in EBSD analysis and has potential for accelerated acquisition and efficient data management discussed below.

4.1. Implications for EBSD data acquisition and management

The reconstruction results (Section 3.1) show that a complete EBSD dataset can be regenerated at the Kikuchi-pattern level from a trained TF-INR model with low error in both pattern intensity and indexed orientation. Since reconstruction requires only the SIREN weights and the basis tensor \mathbf{B} , the trained model is itself a compact surrogate of the dataset. For the two datasets studied here, storing the SIREN weights and 512 bases in place of the raw patterns reduces the disk footprint from about 25 GB to 35 MB – 715× compression of 16-bit 120×120 patterns.

This matters in practice because advanced EBSD workflows need the full Kikuchi patterns: from dictionary indexing to the autoencoder methods (Section 1). Yet the patterns are routinely discarded once orientations have been extracted, especially in

high-throughput industrial settings where the storage burden quickly becomes prohibitive. A trained TF-INR offers a way to preserve pattern-level information at a fraction of the storage. The same property eases data sharing and archiving: an operator can fit a TF-INR on site to a target accuracy and deposit only the model weights, from which collaborators reconstruct the full patterns on demand and run downstream analysis. It is for this reason, we trained and evaluated the models on *raw* patterns (without background subtraction or other preprocessing) so that users have the flexibility to apply any processing pipeline of preference, including methods yet to be developed.

Super-resolution (Section 3.2) presents another opportunity for enhancing experimental EBSD workflows. As resolution is limited by the acquisition time, an initial coarse-grid scan could train a TF-INR model that upscales the map and guides a finer follow-up measurement to regions of interest: boundaries, triple junctions, or sites of potential damage initiation such as fatigue cracks [49, 50]. The unified boundary and defect localization by dif-

ferentiation (Section 3.3) could support such workflows.

4.2. New capabilities for microstructure analysis

The diffraction gradient $S(x, y)$ is the clearest illustration of the advantages of treating EBSD as a continuous, differentiable field. It analytically locates the positions where the Kikuchi field varies most rapidly in the specimen frame and thereby provides a single map that exposes both grain boundaries and intragranular heterogeneity. For boundary localization it requires neither pattern indexing nor disorientation-based segmentation. The boundary network appears as a continuously varying scalar tied neither to the measurement grid nor to any chosen disorientation threshold.

A further benefit is robustness to common EBSD artifacts such as scratches, surface contamination, and non- or mis-indexed points. Since the representation encodes the whole field (instead of discrete points), derived fields, including $S(x, y)$, stay coherent where individual measurements are locally corrupted (Figure 7). The local corruption or polishing artifacts can lead to erroneously identified grain boundaries with conventional workflows (see arrow in the AM718 close-up in Figure 7). The diffraction gradient field does not include this artifact in the AM718 case but shows elevated intensity within grains in the RX718 microstructure. This difference is likely associated with the use of the same rank ($R = 512$) for both microstructures, while PCA of AM718 dataset suggests that a greater number of bases is needed to capture the same variance (close to 95%) as for RX718 (Figure 8a). These results imply potential for fine-tuning the rank for denoising EBSD without a significant sacrifice in reconstruction accuracy. For boundary localization, only visual results are demonstrated in this study, quantitative microstructure analysis (e.g., grain size distributions) could follow by segmentation of the diffraction gradient field with such algorithms as watershed [51, 52].

Reconstruction is also not confined to the acquisition grid (Section 3.2). The coefficient field $\mathbf{A}(x, y)$ can be evaluated anywhere within the scanned region. Beyond the super-resolution test used here for evaluation (Figure 5), this capability supports such EBSD post-processing tasks as filling non-indexed points or converting between grid types (square vs. hexagonal). Existing tools for these tasks act on orientations extracted from the patterns. The present approach makes them available at the raw

pattern level and offers the choice on subsequent indexing or other analyses needing full patterns, instead of extracted and inherently lossy quantities.

Finally, the arbitrary-path query (Section 3.2) gives access to sub-grid diffraction variation. Across a boundary, the reconstructed patterns show the features of one grain weakening as those of the neighbor strengthen, which is a behavior consistent with Kikuchi diffraction from two (or more) lattices within the interaction volume of the beam [46, 47]. Overlapping diffraction is known to degrade pattern quality and to cause indexing ambiguity or failure in Hough-based workflows [53, 54]. Neural queries of the patterns reproduce this trend, as demonstrated with the indexing confidence metric (Figure 6c). We emphasize that the pattern reconstruction from TF-INR at arbitrary locations is a direct consequence of the learned continuous representation instead of being a post-processing operation such as pixel-wise interpolation of a pair of images.

4.3. Limitations

While powerful, the neural EBSD framework and its present implementation have limitations.

First, the current approach trains a TF-INR instance for every individual EBSD dataset from scratch. For the datasets studied here, TF-INR with $R = 512$ takes about 3 h to reach the reported accuracy on a workstation with NVIDIA RTX A4000. While long-term storage benefits discussed above are evident, they need investment in training time and compute. Integration with pattern dictionaries [5] as fixed (non-learnable) bases or pre-training the representation on similar microstructures could reduce the computational cost of training from scratch considered here.

Second, the rank of the model R is microstructure-dependent. In this study focused on single-phase f.c.c. alloys in two conditions, the fixed rank of $R = 512$ achieved faithful reconstruction even though this rank falls slightly short of capturing 95% of variance in case of PCA (Figure 8a). The rank may need to be higher for strongly deformed, ultrafine-grained, or multiphase materials, which would increase the number of bases to store and the computational cost of training with the current approach. Building on the PCA-based guidance used here, further developments could devise a procedure for automated rank determination for any given EBSD dataset

with a target explained variance or reconstruction accuracy.

Third, off-grid reconstructions that demonstrate super-resolution and sampling along arbitrary paths (Section 3.2) represent inference from the model. The super-resolution test emulated coarse-grid measurement for which ground-truth patterns were available on a finer grid and thus offered quantitative validation (Figure 5). At the same time, while the diffraction evolution across boundaries showed physically realistic transitions and overlap of Kikuchi patterns, this behavior needs further validation by high-resolution EBSD or other methods, e.g., transmission Kikuchi diffraction [55, 56].

Finally, while the diffraction gradient $S(x, y)$ provides effective boundary and defect localization, its current implementation should be used with two caveats. The coefficient fields \mathbf{A} are defined only up to the scaling fixed by the basis regularization and initialization, so their spatial derivatives carry no absolute scale. The magnitude is therefore interpretable in a relative sense within a single trained representation without quantitative comparison between maps. In addition, $S(x, y)$ combines all sources of pattern change into a single scalar, which includes orientation, band sharpness, and contrast. While its magnitude displays continuously varying "strength" of the diffraction discontinuity (even within a single trace Figure 7), it does not explicitly relate to physically intuitive characteristics such as crystallographic misorientation or boundary character. This limitation could be addressed by analyzing the derivatives of individual coefficients A_r obtained with bases tied to a simulated pattern dictionary [5]. Another option is a hybrid analysis where $S(x, y)$ identifies regions of interest with strong discontinuity for targeted indexing and conventional crystallographic analysis (or even additional fine-grid measurement).

5. Conclusions

We introduced neural EBSD, a compact and differentiable framework that treats a spatially resolved EBSD dataset as a continuous Kikuchi diffraction field instead of a set of independent patterns fixed to the acquisition grid. Demonstration and evaluation on recrystallized (RX718) and additively manufactured (AM718) Inconel 718 resulted in the following findings.

1. Faithful representation with factorization. The factorized formulation (TF-INR) achieves

more accurate representation of EBSD data than the joint formulation (4D-INR) in the present implementations.

2. High-ratio compression. The trained model is a compact surrogate for the EBSD dataset: storing its weights and learned bases in place of the raw patterns gives a 715-fold reduction in size with the full patterns reconstructable on demand.
3. Full-pattern super-resolution. The continuity of the representation lets it recover patterns at unmeasured positions; trained on a quarter of the scan points, TF-INR reconstructed the withheld patterns such that 97% of indexed orientations in the RX718 case were within 4° of the reference.
4. Sub-grid query. Neural EBSD enables pattern sampling between measured grid points: querying four positions between adjacent scan points refines the spatial resolution five-fold along a chosen path and reproduces smooth pattern transitions across grain boundaries.
5. Indexing-free boundary localization. Differentiating the coefficient fields yields a diffraction gradient field, $S(x, y)$, continuous in the specimen frame and free of both indexing and thresholds; it recovers the boundary network in RX718 and, in AM718, both the grain boundaries and intragranular heterogeneity.

These findings demonstrate the potential of neural EBSD as a practical pattern-native framework for storing and analyzing spatially-resolved diffraction data. Natural extensions include three-dimensional EBSD, multiphase materials, and INR-in-the-loop workflows for efficient experimental data acquisition.

6. Methods

6.1. Materials

EBSD datasets used here were originally collected by Calvat et al. [21] on a Thermo Fisher SEM EDAX OIM-Hikari detector with an accelerating voltage of 20 kV, current of 6.4 nA, and exposure time of 8.5 ms per diffraction pattern at 12 mm of working distance and a 70° tilt. The chemical composition, processing history, and additional characterization details are given by Calvat et al. [18, 21].

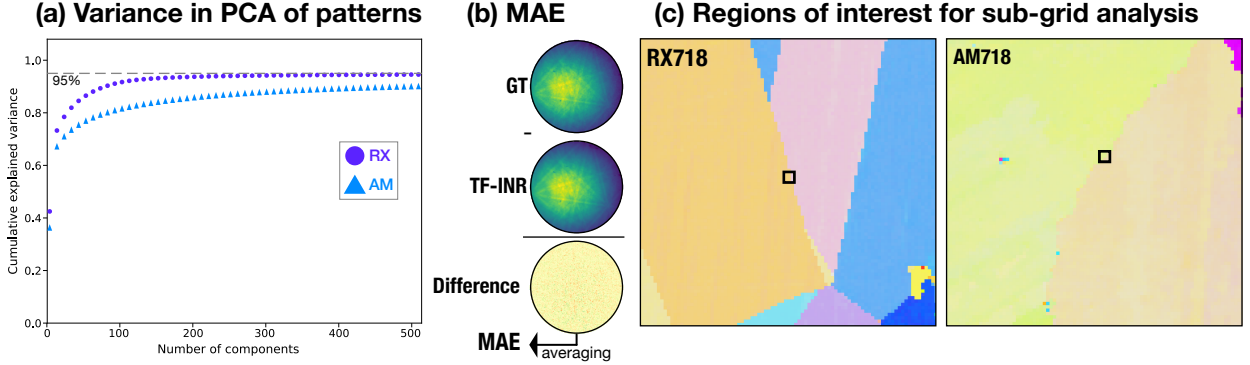


Figure 8: (a) Explained variance of randomly sampled 200 000 patterns from the two EBSD datasets; (b) visual illustration of pattern-level MAE; (c) regions of interest showing the location of 3×3 windows for sub-grid sampling in Figure 6.

6.2. Architecture and training

The two formulations in Section 2.2 use distinct architectures.

4D-INR. The 4D-INR network implementing the joint formulation (Equation (2)) has five SIREN layers of width 256: input layer with frequency $\omega_0^{(1)} = 30$, and hidden layers with frequency $\omega_0^{(h)} = 30$. To increase the capacity of the monolithic network for detector space band structure, the detector coordinates (u, v) are additionally lifted using a random Fourier feature map with $m = 256$ frequencies sampled from $\mathcal{N}(0, \sigma^2)$ with $\sigma = 3.0$. The Fourier features are concatenated with the raw coordinates, giving an effective input dimensionality of $4 + 2m = 516$.

To stabilize optimization of the joint 4D field, training uses a detector coordinate scaling curriculum. Specifically, the detector coordinates are rescaled by a factor that increases linearly from 0.25 to 1.0 over the first 20 000 optimization steps, so that the model first fits the coarse pattern structure before resolving the full detector coordinate variation. The total training objective is a weighted pixel reconstruction loss, $\mathcal{L}_{\text{total}} = \mathcal{L}_{\text{pixel}}$, where detector pixels identified as high frequency band region (top 15% of gradient magnitude) pixels are assigned weight $w = 2$ and background pixels are assigned weight $w = 1$. Optimization uses Adam with learning rate 10^{-4} and a batch size of 32 768 sampled specimen-detector coordinates for up to 200 000 steps. Gradients are clipped to a maximum norm of 1.0. The learning rate is decayed by a factor of 0.5 every 40 000 steps, and early stopping is applied with patience 30, evaluated every 1000 steps with a minimum improvement threshold of $\delta = 2 \times 10^{-5}$.

TF-INR. In TF-INR implementing the factorized representation (Equation (3)), the coefficient field $A(x, y)$ is parameterized by five SIREN layers of width 512, first layer frequency $\omega_0^{(1)} = 30$, and hidden layer frequency $\omega_0^{(h)} = 30$. The network outputs $R - 1$ learned coefficients, and a constant leading coefficient of unity is prepended so that the full coefficient vector satisfies $\mathbf{a}(x, y) \in \mathbb{R}^R$. In all experiments in this study, the rank is fixed at $R = 512$.

The detector basis is represented explicitly as a learnable tensor $B \in \mathbb{R}^{R \times H_p \times W_p}$, where $H_p = 120$ and $W_p = 120$ are the height and width of the patterns used in this study. The first basis image is initialized as the empirical mean Kikuchi pattern, so the fixed leading coefficient preserves the average pattern across the dataset. The remaining basis images are initialized from leading principal components obtained with PCA of a random subsample of up to 200 000 training patterns. All basis images are then optimized jointly with the SIREN weights. Thus, PCA provides a data-informed initialization of the dominant Kikuchi pattern modes, while the final detector basis remains fully trainable.

Training follows the objective in Equation (7) with $\lambda_B = 10^{-6}$. Detector pixels identified as high-frequency band-region pixels during preprocessing are assigned weight $w = 2$, while background pixels are assigned weight $w = 1$ (following the same weighting scheme as 4D-INR). To emphasize physically informative Kikuchi-band features without losing global detector coverage, the fraction of high-frequency detector pixels in each mini-batch is clipped to $[0.15, 0.50]$. Optimization uses Adam with learning rate 10^{-4} and a batch size of 32 768 sampled specimen-detector coordinates for

up to 200 000 steps. A `ReduceLROnPlateau` scheduler with factor 0.5, patience 10, and minimum learning rate 10^{-6} is activated after 4000 warm-up steps. Training is stopped early if the validation loss does not improve by more than $\delta = 10^{-5}$ for 30 consecutive evaluations.

6.3. Evaluation metrics

We evaluate the reconstruction quality of the INR models using pattern level intensity error and orientation consistency.

Mean absolute error (MAE). Let $I(x, y, u, v)$ denote the reference experimental Kikuchi pattern intensity, and $\hat{I}(x, y, u, v)$ denote the corresponding INR-reconstructed intensity. Detector pixels are evaluated within the circular aperture mask \mathcal{M} .

The mean absolute error (MAE) per pattern (Figure 8b) is defined as

$$\text{MAE}(x, y) = \frac{1}{|\mathcal{M}|} \sum_{(u,v) \in \mathcal{M}} \left| \hat{I}(x, y, u, v) - I(x, y, u, v) \right|. \quad (9)$$

The map-averaged MAE is then computed by averaging over all scan positions,

$$\overline{\text{MAE}} = \frac{1}{N} \sum_{(x,y)} \text{MAE}(x, y). \quad (10)$$

where N is the total number of scan points.

Orientation deviation. For Hough indexing, both experimental and reconstructed Kikuchi patterns were Gaussian bandpass filtered to reduce background, using $\sigma_{\text{low}} = 0.25$ and $\sigma_{\text{high}} = 0.035$ in Nyquist frequency units [12]

For each scan point (x, y) , two orientations are obtained: one, g_{ref} , by Hough indexing of the measured Kikuchi pattern (reference) and one, g by Hough indexing of the reconstructed pattern from neural representation. The orientation deviation, $\Delta\theta$, is computed in MTEX [42] as:

$$\Delta\theta(x, y) = \angle(g_{\text{ref}}^{-1}g), \quad (11)$$

where $\angle(\cdot)$ denotes the symmetry-reduced rotation angle under the cubic point group.

Confidence metric. Hough indexing also returns a confidence metric for each pattern, which measures how strongly the best orientation solution is favored over competing solutions in the band-voting step (normalized to $[0,1]$). Low values indicate ambiguous patterns, such as those formed by overlapping diffraction from two grains near a boundary [41, 40]. We compute the confidence metric in `kikuchipy` and use in Sections 3.2 and 3.3 to track diffraction ambiguity along sub-grid paths.

Acknowledgments

The authors thank Drs. J.C. Stinville and Mathieu Calvat at UIUC and Drs. Pascal Thome and I-Ting Ho at the University of Arizona for insightful discussions.

References

- [1] A. J. Schwartz, M. Kumar, B. L. Adams, D. P. Field, Electron backscatter diffraction in materials science, Vol. 2, Springer, 2009.
- [2] A. J. Wilkinson, T. B. Britton, Strains, planes, and EBSD in materials science, *Materials today* 15 (9) (2012) 366–376.
- [3] K. Kunze, S. Wright, B. L. Adams, D. J. Dingley, Advances in automatic ebsp single orientation measurements, *Texture, Stress, and Microstructure* 20 (1-4) (1993) 41–54.
- [4] N. Krieger Lassen, Automatic localisation of electron backscattering pattern bands from hough transform, *Materials Science and Technology* 12 (10) (1996) 837–843.
- [5] Y. H. Chen, S. U. Park, D. Wei, G. Newstadt, M. A. Jackson, J. P. Simmons, M. De Graef, A. O. Hero, A dictionary approach to electron backscatter diffraction indexing, *Microscopy and Microanalysis* 21 (3) (2015) 739–752.
- [6] F. Bachmann, R. Hielscher, H. Schaeben, Grain detection from 2D and 3D EBSD data—specification of the MTEX algorithm, *Ultramicroscopy* 111 (12) (2011) 1720–1733.
- [7] W. Pantleon, Resolving the geometrically necessary dislocation content by conventional electron backscattering diffraction, *Scripta Materialia* 58 (11) (2008) 994–997.
- [8] S. I. Wright, M. M. Nowell, D. P. Field, A review of strain analysis using electron backscatter diffraction, *Microscopy and microanalysis* 17 (3) (2011) 316–329.
- [9] M. Kamaya, Assessment of local deformation using EBSD: Quantification of local damage at grain boundaries, *Materials characterization* 66 (2012) 56–67.
- [10] D. M. Saylor, B. S. El-Dasher, B. L. Adams, G. S. Rohrer, Measuring the five-parameter grain-boundary distribution from observations of planar sections, *Metallurgical and Materials Transactions A* 35 (7) (2004) 1981–1989.

- [11] F. Wang, J.-C. Stinville, M. Charpagne, M. P. Echlin, S. R. Agnew, T. M. Pollock, M. De Graef, D. S. Gianola, Dislocation cells in additively manufactured metallic alloys characterized by electron backscatter diffraction pattern sharpness, *Materials Characterization* 197 (2023) 112673.
- [12] P. Thome, S. Medghalchi, J. Frenzel, J. Schreuer, G. Eggeler, Ni-base superalloy single crystal (sx) mosaicity characterized by the rotation vector base line electron back scatter diffraction (rvb-ebbsd) method, *Ultramicroscopy* 206 (2019) 112817.
- [13] L. N. Brewer, P. G. Kotula, J. R. Michael, Multivariate statistical approach to electron backscattered diffraction, *Ultramicroscopy* 108 (6) (2008) 567–578.
- [14] A. J. Wilkinson, D. M. Collins, Y. Zayachuk, R. Korla, A. Vilalta-Clemente, Applications of multivariate statistical methods and simulation libraries to analysis of electron backscatter diffraction and transmission kikuchi diffraction datasets, *Ultramicroscopy* 196 (2019) 88–98.
- [15] T. P. McAuliffe, D. Dye, T. B. Britton, Spherical-angular dark field imaging and sensitive microstructural phase clustering with unsupervised machine learning, *Ultramicroscopy* 219 (2020) 113132.
- [16] A. Chauniyal, P. Thome, M. Stricker, Employing constrained nonnegative matrix factorization for microstructure segmentation, *Microscopy and Microanalysis* 30 (4) (2024) 712–723.
- [17] Z. T. Varley, G. S. Rohrer, M. De Graef, Accelerating dictionary indexing of electron backscatter diffraction patterns with pca and quantization, *Scientific Reports* 16 (2026) 4382.
- [18] M. Calvat, C. Bean, D. Anjaria, H. Park, H. Wang, K. Vecchio, J. Stinville, Learning metal microstructural heterogeneity through spatial mapping of diffraction latent space features, *npj Computational Materials* 11 (1) (2025) 284.
- [19] Y.-C. Liu, C.-K. Yeh, S.-P. Tsai, P.-Y. Tung, Learning crystallographic orientations from electron backscatter diffraction patterns using variational autoencoder, *Cell Reports Physical Science* 6 (10).
- [20] J. Wang, M. Calvat, J. C. Stinville, M. I. Latypov, Lattice genome: representation and analysis of heterogeneous crystalline microstructures, *arXiv:2606.09611* (2026).
- [21] M. Calvat, D. Anjaria, H. Wang, K. Vecchio, J.-C. Stinville, Kikuchi pattern dataset from wrought and as-built additively manufactured superalloys (Sep. 2025). [doi:10.5061/DRYAD.ZCRJDFNR9](https://doi.org/10.5061/DRYAD.ZCRJDFNR9).
- [22] M. I. Latypov, M. Kühbach, I. J. Beyerlein, J.-C. Stinville, L. S. Toth, T. M. Pollock, S. R. Kalidindi, Application of chord length distributions and principal component analysis for quantification and representation of diverse polycrystalline microstructures, *Materials Characterization* 145 (2018) 671–685.
- [23] B. Mildenhall, P. P. Srinivasan, M. Tancik, J. T. Barron, R. Ramamoorthi, R. Ng, Nerf: Representing scenes as neural radiance fields for view synthesis, *Communications of the ACM* 65 (1) (2021) 99–106.
- [24] J. J. Park, P. Florence, J. Straub, R. Newcombe, S. Lovegrove, DeepSDF: Learning continuous signed distance functions for shape representation, in: *Proceedings of the IEEE/CVF conference on computer vision and pattern recognition*, 2019, pp. 165–174.
- [25] V. Sitzmann, J. Martel, A. Bergman, D. Lindell, G. Wetzstein, Implicit neural representations with periodic activation functions, *Advances in neural information processing systems* 33 (2020) 7462–7473.
- [26] Y. Strümler, J. Postels, R. Yang, L. Van Gool, F. Tombari, Implicit neural representations for image compression, in: *Computer Vision – ECCV 2022: 17th European Conference, Tel Aviv, Israel, October 23–27, 2022, Proceedings, Part XXVI*, Springer-Verlag, 2022, pp. 74–91.
- [27] M. Pezzoli, F. Antonacci, A. Sarti, Implicit neural representation with physics-informed neural networks for the reconstruction of the early part of room impulse responses, in: *Proceedings of the 10th Convention of the European Acoustics Association Forum Acusticum 2023*, European Acoustics Association, 2023, pp. 2177–2184.
- [28] P. Xie, Y. Liu, C. Liu, C. Song, X. Zhang, Simultaneous suppression of seismic random and erratic noise using PINN with high-frequency preservation, *Journal of Geophysics and Engineering* 22 (6) (2025) 1796–1808.
- [29] B. Mildenhall, P. Hedman, R. Martin-Brualla, P. P. Srinivasan, J. T. Barron, Nerf in the dark: High dynamic range view synthesis from noisy raw images, in: *Proceedings of the IEEE/CVF conference on computer vision and pattern recognition*, 2022, pp. 16190–16199.
- [30] J. Xu, D. Moyer, B. Gagoski, J. E. Iglesias, P. E. Grant, P. Golland, E. Adalsteinsson, Nesvor: implicit neural representation for slice-to-volume reconstruction in mri, *IEEE transactions on medical imaging* 42 (6) (2023) 1707–1719.
- [31] S. Ye, L. Shen, M. T. Islam, L. Xing, Super-resolution biomedical imaging via reference-free statistical implicit neural representation, *Physics in Medicine & Biology* 68 (20) (2023) 205020.
- [32] A. Molaie, A. Aminimehr, A. Tavakoli, A. Kazerouni, B. Azad, R. Azad, D. Merhof, Implicit neural representation in medical imaging: A comparative survey (2023). [arXiv:2307.16142](https://arxiv.org/abs/2307.16142).
- [33] Y. Moussaoui, D. Mateus, N. Taheri, S. Moussaoui, S. Carlier, Thomas an Stute, Implicit neural representations for end-to-end pet reconstruction, in: *2025 IEEE 22nd International Symposium on Biomedical Imaging (ISBI)*, 2025, pp. 1–5, hAL Id: hal-04999198. [doi:10.1109/ISBI60581.2025.10980961](https://doi.org/10.1109/ISBI60581.2025.10980961).
- [34] C.-M. Hsu, S. Xu, M. J. Lynch, Y. Wang, X. Liu, C. Williams, X. Wang, L. Qian, K. G. Field, X. Qian, INR-TEM: Robust cavity detection in multifocus tem images via implicit neural representations, *APL Machine Learning* 4 (1).
- [35] A. Chen, Z. Xu, A. Geiger, J. Yu, H. Su, TensorRF: Tensorial radiance fields, in: *Computer Vision – ECCV 2022*, Springer, 2022, pp. 333–350.
- [36] Y. Xie, T. Takikawa, S. Saito, O. Litany, S. Yan, N. Khan, F. Tombari, J. Tompkin, V. Sitzmann, S. Sridhar, Neural fields in visual computing and beyond, *Computer Graphics Forum* 41 (2) (2022) 641–676.
- [37] Y. Chen, S. Liu, X. Wang, Learning continuous image representation with local implicit image function, in: *2021 IEEE/CVF Conference on Computer Vision and Pattern Recognition (CVPR)*, 2021, pp. 8624–8634.
- [38] L. Mescheder, M. Oechsle, M. Niemeyer, S. Nowozin, A. Geiger, Occupancy networks: Learning 3D reconstruction in function space, in: *2019 IEEE/CVF Conference on Computer Vision and Pattern Recognition*

- (CVPR), 2019, pp. 4455–4465.
- [39] T. Müller, A. Evans, C. Schied, A. Keller, Instant neural graphics primitives with a multiresolution hash encoding, *ACM transactions on graphics (TOG)* 41 (4) (2022) 1–15.
- [40] H. W. Ånes, L. A. H. Lervik, O. Natlandsmyr, T. Bergh, E. Prestat, A. Gerlt, A. V. Bugten, E. M. Østvold, Z. Xu, C. Francis, M. Nord, pyxem/kikuchipy: kikuchipy 0.11.5 (2026).
- [41] S. I. Wright, B. L. Adams, Automatic analysis of electron backscatter diffraction patterns, *Metallurgical Transactions A* 23 (1992) 759–767.
- [42] F. Bachmann, R. Hielscher, H. Schaeben, Texture analysis with MTEX—free and open source software toolbox, *Solid state phenomena* 160 (2010) 63–68.
- [43] R. Krakow, R. J. Bennett, D. N. Johnstone, Z. Vukmanovic, W. Solano-Alvarez, S. J. Lainé, J. F. Einsle, P. A. Midgley, C. M. F. Rae, R. Hielscher, On three-dimensional misorientation spaces, *Proceedings of the Royal Society A: Mathematical, Physical and Engineering Sciences* 473 (2206) (2017) 20170274.
- [44] Z. Ding, E. Pascal, M. De Graef, Indexing of electron back-scatter diffraction patterns using a convolutional neural network, *Acta Materialia* 199 (2020) 370–382.
- [45] Q. Shi, Y. Zhou, H. Zhong, D. Loinsard, C. Dan, F. Zhang, Z. Chen, H. Wang, S. Roux, Indexation of electron diffraction patterns at grain boundaries, *Materials Characterization* 182 (2021) 111553.
- [46] V. Tong, J. Jiang, A. J. Wilkinson, T. B. Britton, The effect of pattern overlap on the accuracy of high resolution electron backscatter diffraction measurements, *Ultramicroscopy* 155 (2015) 62–73.
- [47] K. Marquardt, M. De Graef, S. Singh, H. Marquardt, A. Rosenthal, S. Koizumi, Quantitative electron backscatter diffraction (ebbsd) data analyses using the dictionary indexing (di) approach: Overcoming indexing difficulties on geological materials, *American Mineralogist* 102 (9) (2017) 1843–1855.
- [48] S. Patala, C. A. Schuh, A continuous and one-to-one coloring scheme for misorientations, *Acta materialia* 59 (2) (2011) 554–562.
- [49] M. I. Latypov, J.-C. Stinville, J. R. Mayeur, J. M. Hestroffer, T. M. Pollock, I. J. Beyerlein, Insight into microstructure-sensitive elastic strain concentrations from integrated computational modeling and digital image correlation, *Scripta Materialia* 192 (2021) 78–82.
- [50] J.-C. Stinville, W. C. Lenthe, M. P. Echlin, P. G. Callahan, D. Texier, T. M. Pollock, Microstructural statistics for fatigue crack initiation in polycrystalline nickel-base superalloys, *International Journal of Fracture* 208 (1) (2017) 221–240.
- [51] G. Fotos, A. Campbell, P. Murray, E. Yakushina, Deep learning enhanced watershed for microstructural analysis using a boundary class semantic segmentation, *Journal of Materials Science* 58 (2023) 14390–14410.
- [52] S. Beucher, The watershed transformation applied to image segmentation, *Scanning Microscopy* 1992 (6).
- [53] S. Zaefferer, On the formation mechanisms, spatial resolution and intensity of backscatter Kikuchi patterns, *Ultramicroscopy* 107 (2–3) (2007) 254–266.
- [54] F. J. Humphreys, Review grain and subgrain characterisation by electron backscatter diffraction, *Journal of Materials Science* 36 (2001) 3833–3854.
- [55] P. W. Trimby, Orientation mapping of nanostructured materials using transmission kikuchi diffraction in the scanning electron microscope, *Ultramicroscopy* 120 (2012) 16–24.
- [56] R. R. Keller, R. H. Geiss, Transmission ebbsd from 10 nm domains in a scanning electron microscope, *Journal of Microscopy* 245 (3) (2012) 245–251.